

Single-Chain Magnets | Hot Paper |



Michał Rams,^{*[a]} Aleksej Jochim,^[b] Michael Böhme,^[c] Thomas Lohmiller,^[d]
Magdalena Ceglarska,^[a] Marek M. Rams,^[a] Alexander Schnegg,^[d, e] Winfried Plass,^[c] and
Christian Näther^{*[b]}

Abstract: The cobalt(II) in $[\text{Co}(\text{NCS})_2(4\text{-methoxypyridine})_2]_n$ are linked by pairs of thiocyanate anions into linear chains. In contrast to a previous structure determination, two crystallographically independent cobalt(II) centers have been found to be present. In the antiferromagnetic state, below the critical temperature ($T_c = 3.94$ K) and critical field ($H_c = 290$ Oe), slow relaxations of the ferromagnetic chains are observed. They originate mainly from defects in the magnetic structure, which has been elucidated by micromagnetic Monte Carlo simulations and ac measurements using pristine

and defect samples. The energy barriers of the relaxations are $\Delta_{r1} = 44.9(5)$ K and $\Delta_{r2} = 26.0(7)$ K for long and short spin chains, respectively. The spin excitation energy, measured by using frequency-domain EPR spectroscopy, is 19.1 cm^{-1} and shifts 0.1 cm^{-1} due to the magnetic ordering. Ab initio calculations revealed easy-axis anisotropy for both Co^{II} centers, and also an exchange anisotropy J_{xx}/J_{zz} of 0.21. The XXZ anisotropic Heisenberg model (solved by using the density renormalization matrix group technique) was used to reconcile the specific heat, susceptibility, and EPR data.

Introduction

The synthesis of new magnetic coordination compounds and polymers is an important topic in modern coordination chemistry. In this context, numerous compounds have been reported that show a slow relaxation of magnetization, for example, single-molecule magnets (SMMs), single-ion magnets (SIMs), and single-chain magnets (SCMs).^[1] Such compounds

possess magnetic anisotropy and can show an open magnetic hysteresis of purely molecular origin, which allows magnetization to be stored below the so-called blocking temperature.^[1a–g] Therefore, they are potentially interesting for future applications in spintronics or as high-density storage materials.^[2] Whereas SMMs and SIMs usually consist of discrete units, in SCMs the spins are aligned along a so-called spin chain that shows either ferromagnetic (FM) or antiferromagnetic (AF) intrachain coupling. In the case of SCMs, the magnetic properties are based on magnetic domains that form due to intrachain cooperative effects. For the general design of SCMs, it is beneficial to connect paramagnetic cations with large magnetic single-ion anisotropy into chains through bridging ligands that mediate magnetic exchange.^[1a,b] Therefore, many such compounds with cobalt(II), manganese(III), and many other cations have been investigated with a variety of different ligands.^[3]

In addition to intrachain magnetic exchange, interchain magnetic interactions become important for SCMs at lower temperatures, because they lead to the formation of magnetic phases. In this context, we reported on the first AF phase of single-chain magnets based on thiocyanate anions as bridging ligands.^[4] Such behavior had already been reported by Miyasaka et al. in 2010.^[3f] To gain a deeper insight, many compounds of the general formula $[\text{Co}(\text{NCS})_2(\text{L})_2]_n$ have been synthesized by our group using co-ligands L that consist exclusively of pyridine derivatives substituted at the *para* position. In all of these compounds, the cobalt(II) cations are linked into linear chains by pairs of μ -1,3-bridging thiocyanate anions and possess an octahedral $[\text{N}_4\text{S}_2]$ coordination sphere. The basal plane of the latter consists of two *trans*-coordinating nitrogen atoms and two *trans*-coordinating sulfur atoms belonging to the thiocya-

[a] Dr. M. Rams, M. Ceglarska, Dr. M. M. Rams
Institute of Physics, Jagiellonian University
Łojasiewicza 11, 30348 Kraków (Poland)
E-mail: m.rams@uj.edu.pl

[b] A. Jochim, Prof. Dr. C. Näther
Institut für Anorganische Chemie, Christian-Albrechts-Universität zu Kiel
Max-Eyth-Straße 2, 24118 Kiel (Germany)
E-mail: cnaether@ac.uni-kiel.de

[c] M. Böhme, Prof. Dr. W. Plass
Institut für Anorganische und Analytische Chemie
Friedrich-Schiller-Universität Jena, Humboldtstr. 8, 07743 Jena (Germany)

[d] Dr. T. Lohmiller, Dr. A. Schnegg
EPR4Energy Joint Lab, Institut für Nanospektroskopie
Helmholtz-Zentrum Berlin für Materialien und Energie GmbH
Kekuléstr. 5, 12489 Berlin (Germany)

[e] Dr. A. Schnegg
EPR Research Group, MPI for Chemical Energy Conversion
Stiftstraße 34–36, 45470 Mülheim an der Ruhr (Germany)

 Supporting information and the ORCID identification number(s) for the author(s) of this article can be found under:
<https://doi.org/10.1002/chem.201903924>.

 © 2020 The Authors. Published by Wiley-VCH Verlag GmbH & Co. KGaA. This is an open access article under the terms of Creative Commons Attribution NonCommercial-NoDerivs License, which permits use and distribution in any medium, provided the original work is properly cited, the use is non-commercial and no modifications or adaptations are made.

nate ligands and is saturated by two apical *trans*-coordinating pyridine nitrogen atoms of the neutral co-ligands (denoted as all-*trans* coordination). Analysis of the magnetic behavior of all these compounds reveals that they fall into two categories. The compounds of the first group show AF^[5] and those of the second group FM interchain interactions between the individual chains.^[6] In a subsequent report, we presented a similar compound with 4-benzoylpyridine as co-ligands in which each of the thiocyanate nitrogen and sulfur donor atoms are in *cis* positions and the two apical pyridine nitrogen donor atoms in *trans* positions (denoted as *cis-cis-trans* coordination).^[7] For this compound, a similar exchange constant and energy for spin reversal were found as for those compounds with an all-*trans* coordination.^[7] The magnetic data of all of these compounds were analyzed by using an analytical Ising model for a one-dimensional spin chain with an effective spin of $S = 1/2$, in which a strong easy-axis type of single-ion anisotropy as well as a parallel alignment of the easy axes is assumed. For the FM pyridine (py) compound $[\text{Co}(\text{NCS})_2(\text{py})_2]_n$, the presence of easy-axis anisotropy was proven by high-frequency EPR measurements.^[6a] The results of ab initio calculations were in agreement with these findings and predicted that the easy axis should be nearly parallel to the N–N vector of the pyridine co-ligands, which was later experimentally confirmed by neutron diffraction analysis.^[8] As a consequence, this opens up the possibility of modifying and tuning the single-ion anisotropy by changing the apical pyridine-based co-ligands.

However, even though considerable effort has already been made, many challenging questions remain, including the influence of the magnetic field on the ac properties and what is responsible for the relaxations observed in the antiferromagnetic phase. Another question is whether the Ising model is really an adequate approximation, because this might not necessarily be the case, as previously only easy-axis single-ion anisotropy was proven. This latter question may be answered by using a more general model, and this also forms a part of this paper. Moreover, a comparison of the energy barrier determined by EPR spectroscopy without making any model assumptions with those derived by fitting specific heat or susceptibility data using the Ising model is long overdue.

In this context, the results of this contribution represent a milestone for the validation of the employed physical model and go far beyond what has previously been reported for this family of compounds. In line with this, we became interested in 4-methoxypyridine as a co-ligand, which contains a strong donor substituent at the *para* position. We succeeded in the synthesis of several compounds, including the desired chain compound $[\text{Co}(\text{NCS})_2(4\text{-methoxypyridine})_2]_n$ (**1**), which was selected as a model compound. During the course of these investigations, the synthesis, crystal structures, and properties of these same compounds were reported by Mautner et al.^[9] They found an AF interchain interaction and a slow relaxation of the magnetization, frequently observed for this class of SCMs. In their work, the structure determination revealed that only one crystallographically independent cobalt(II) is present and that the 4-methoxypyridine co-ligands are disordered. This is a clear contradiction of our results presented in this work,

which show that the unit cell is clearly doubled leading to two crystallographically independent cobalt(II) and a well-ordered structure. Moreover, we present specific heat measurements and a theoretical study of this compound, from which information on the magnetic exchange and the single-ion anisotropy can be deduced. High-level ab initio calculations rely on accurate structural data, and it is shown that the orientation of the co-ligands plays an important role in the cobalt(II) magnetic single-ion anisotropy. Moreover, frequency-domain Fourier transform THz-EPR (FD-FT THz-EPR) measurements are presented, which have never before been applied to this group of SCMs. From these measurements, the energies of the magnetic excitations can be determined directly, without any analytical model assumptions, and thus can be generally used as a comparison for such compounds.^[10] Finally, in addition to the Ising model, data analysis has also been performed by using the more general XXZ model and the origin of the relaxations in the AF phase has been investigated by Monte Carlo simulations.

Results and Discussion

Synthesis and characterization

The reaction of $\text{Co}(\text{NCS})_2$ with 4-methoxypyridine in ethanol or methanol led to the formation of a compound with the composition $[\text{Co}(\text{NCS})_2(4\text{-methoxypyridine})_2]_n$ (**1**), for which the CN stretching vibration of the anionic ligands is observed at 2101 cm^{-1} , which indicates the presence of bridging thiocyanate anions (see Figure S1 in Supporting Information). Comparison of the experimental powder X-ray diffraction (PXRD) pattern with that calculated for the chain compound $[\text{Co}(\text{NCS})_2(4\text{-methoxypyridine})_2]_n$ reported recently^[9] indicates that the same crystalline phase was formed (see Figure S2). However, there are some additional weak reflections, which, at first sight, are indicative of some contamination. Closer analysis revealed that the unit cell must be doubled (see below), and in this case, perfect agreement between the experimental and calculated patterns was observed, thereby proving the formation of a pure phase (see Figure S2). It is noted that two additional compounds with the composition $[\text{Co}(\text{NCS})_2(4\text{-methoxypyridine})_4]$ (**2**) and $[\text{Co}(\text{NCS})_2(4\text{-methoxypyridine})_2]$ (**3**) were also obtained, for which the CN stretch is observed at 2063 and 2055 cm^{-1} , respectively, which indicates the presence of only terminally bonded anionic ligands (see Figure S3). PXRD measurements proved that the structures of **2** and **3** correspond to octahedral and tetrahedral complexes, respectively, as previously reported (see Figure S4).^[9] It is noted that pure samples of the tetrahedral complex **3** can be obtained in very short reaction times, which indicates that this compound is formed under kinetic control. To identify which of the two isomers **1** and **3** is thermodynamically stable, a solvent-mediated conversion experiment was performed in which a mixture of both isomers, with an excess of the solid phases, was stirred for 1 day and the precipitates that formed were investigated by PXRD. It was found that all the crystals of compound **3** had disappeared,

thereby proving that the chain compound **1** is the thermodynamically stable isomer at room temperature (see Figure S5).

Thermal properties

To investigate the thermal properties of all the compounds and to ascertain whether compound **1** or **3** or additional 4-methoxypyridine-deficient compounds are obtained as intermediates, as is usually observed for such compounds, several simultaneous thermogravimetry and differential scanning calorimetry (TG-DSC) measurements were performed.^[11] Some TG measurements on **1–3** have already been reported, but the intermediates obtained after each mass step were not characterized and some differences with the present measurements became clear.^[9] It can be noted that up to 400 °C, two mass losses occur for all the compounds, with a strong influence of the heating rate observed, which indicates that the solid-state kinetics play an important role in their thermal decomposition. From the measurements of the 4-methoxypyridine-rich compound **2**, there is no hint that the chain compound **1** is formed as an intermediate, and the residues obtained after the first mass step are always amorphous and contain only terminally coordinated anionic ligands. Interestingly, there is evidence that the tetrahedral complex **3** melts, which is rarely observed for coordination compounds.^[12] As the thermal properties of the compounds are not the focus of the present investigations, a more detailed description is given in the Supporting Information (see Figures S6–S20).

Crystal structure

The crystal structures of compounds **1–3** have already been reported^[9], but the PXRD investigation of compound **1** indicates that the unit cell might be larger. For this compound, a triclinic unit cell with $a = 5.6086(13)$, $b = 8.2371(13)$, $c = 10.248(2)$ Å, $\alpha = 102.823(8)$, $\beta = 104.377(6)$, $\gamma = 101.673(4)^\circ$, and $V = 430.25(15)$ Å³ measured at 100 K has been reported.^[9] The centrosymmetric space group $P\bar{1}$ was found with one crystallographically independent cobalt(II) in the asymmetric unit that is located at a center of inversion. The six-membered rings of the 4-methoxypyridine ligands are disordered in two orientations along the chain. In contrast, the indexing of the diffraction pattern in our investigation leads to a unit cell volume that is twice as large (Table 1). Analysis of the diffraction intensities shows that all the reflections $h0l$, with $h+l=2n+1$, are clearly present, but weaker, indicative of a pseudo- B -centering, which may have been accidentally overlooked in the single-crystal XRD analysis (see Figure S21 and Table S1 in the Supporting Information). If these reflections are not considered in the cell determination, the smaller unit cell is obtained. Because the measurements in this study were performed at higher temperatures, a low-temperature phase transition can be excluded and long-time PXRD measurements proved that the larger cell is already present at room temperature (see Figure S2). However, compound **1** crystallizes in the triclinic space group $P\bar{1}$ with $Z=2$. The asymmetric unit consists of two thiocyanate anions and two 4-methoxypyridine ligands in general positions as

Table 1. Selected crystal data and details of the structure refinement for **1**.

Compound	1
formula	C ₁₄ H ₁₄ N ₄ CoO ₂ S ₂
M [g mol ⁻¹]	393.34
crystal system	triclinic
space group	$P\bar{1}$
a [Å]	8.9702(5)
b [Å]	10.4183(7)
c [Å]	10.8645(7)
α [°]	66.200(5)
β [°]	67.928(5)
γ [°]	82.794(5)
V [Å ³]	860.49(10)
T [K]	170(2)
Z	2
D_{calcd} [g cm ⁻³]	1.518
μ [mm ⁻¹]	1.252
θ_{max} [°]	28.005
measured refl.	13839
unique refl.	4147
refl. $F_0 > 4\sigma(F_0)$	3393
parameter	214
R_{int}	0.0430
R_1 [$F_0 > 4\sigma(F_0)$]	0.0435
wR_2 [all data]	0.1221
GOF	1.015
$\Delta\rho_{\text{max/min}}$ [e Å ⁻³]	0.623/−0.811

well as two crystallographically independent cobalt(II) that are located at centers of inversion (see Table S1 and Figure S22). The cobalt(II) are octahedrally coordinated by two *trans* 4-methoxypyridine molecules and four μ -1,3-bridging thiocyanate anions, with the two nitrogen atoms and the two sulfur atoms in *trans* positions (Figure 1, Figure S23, and Table S2).

Although the pyridine planes of opposing 4-methoxypyridine molecules are coplanar because of inversion symmetry, the corresponding planes of neighboring 4-methoxypyridine molecules are nearly perpendicular, with an angle of 86.462° between the planes of the six-membered rings (Figure 1,

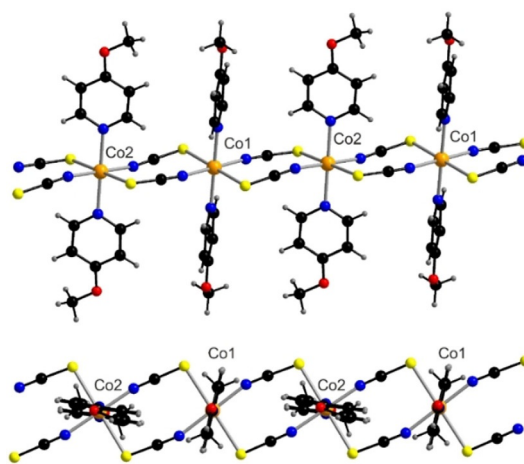


Figure 1. Side view (top) and top view (bottom) of a chain of **1** (Co: orange; S: yellow; N: blue; C: black; O: red; H: gray). An ORTEP plot of **1** can be found in Figure S22 in the Supporting Information.

bottom). The presence of two crystallographically independent cobalt(II) entails two different sets of $N_{py}-N_{py}$ vectors, which are slightly tilted against each other by $7.233(6)^\circ$, thereby leading to a canted arrangement along the chains. In the crystal structure, the $N_{py}-N_{py}$ vectors of neighboring chains are nearly parallel, which corresponds to one of the two different arrangements of chains in the crystal structures of this class of chain compounds. Between the chains, weak C—H...S and C—H...O interactions are observed (see Figure S24 and Table S3 in the Supporting Information).

Specific heat

The specific heat, C , of **1** was measured in the range 2–40 K, and the corresponding data are shown in Figure 2. The peak of $C(T)$ at the critical temperature $T_c = 3.94(1)$ K clearly marks a magnetic ordering transition. The data above T_c were analyzed by using the Ising chain model with the Hamiltonian as in Equation (1).

$$\hat{H} = -J_{\text{Ising}} \sum_i s_i^z s_{i+1}^z \quad (1)$$

The effective spins $s = 1/2$ of the ground Kramers doublet (KD) of cobalt(II) are coupled by an effective exchange interaction, J_{Ising} , through (NCS)₂ bridges (see further sections for the justification of the effective spin $s = 1/2$ and the use of the Ising model). The magnetic contribution to the specific heat (Figure 2), which is obtained by subtracting the lattice contribution from the experimental data, is very well reproduced within this model with $J_{\text{Ising}} = 21.7(2)$ cm⁻¹. Other parameters simultaneously fitted in this analysis describe the lattice contribution, which is estimated by using a linear combination of Debye and Einstein models with fitted amplitude coefficients. Such an approximation of the phonon density of states includes the acoustic phonons essential at low T , but also optical

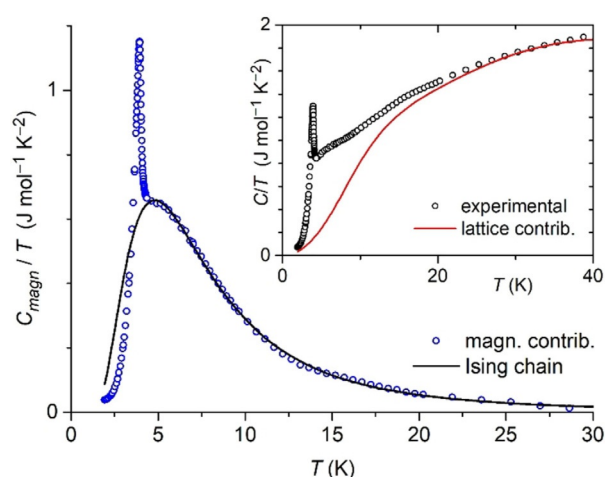


Figure 2. Temperature dependence of the magnetic contribution of specific heat, C_{magn} , of **1**, presented as C_{magn}/T (blue points) and compared with a fit based on the Ising chain model (black line). Inset: Temperature dependence of the specific heat, C , presented as C/T (black points) and the fitted lattice contribution (red line).

phonons of the lowest energy. The latter are essential to reproduce the experimental data up to 40 K. The characteristic phonon temperatures are $\theta_E = 150.3(2)$ K and $\theta_D = 72.3(3)$ K, the dimensionless amplitudes of these contributions are $a_E = 4.16(6)$ and $a_D = 1.84(2)$, and the amplitude of the magnetic contribution is fixed at the expected value. For comparison with experimental vibrational transitions, see Figure S40 in the Supporting Information. Data in the range 4.5–40 K were used for fitting.

Static magnetic properties

The basic magnetic properties of our samples of **1** are similar to those reported by Mautner et al.^[9] and those previously reported for compounds with vinylpyridine and benzoylpyridine as co-ligands.^[7] Here, we only briefly summarize the magnetic properties of **1** and focus on a careful examination of the parameters that are different from those previously reported and compare these with EPR and specific heat data, ab initio calculations and Monte Carlo (MC) micromagnetic simulations.

The FM interaction between the cobalt cations leads to a strong increase in the magnetic susceptibility and the temperature product, χT , at low temperature (see Figure S25 in the Supporting Information). At low field, the maximum of the susceptibility is found at 4.05 K (see Figure S26), and $d(\chi T)/dT$ has its maximum at 3.95(5) K, in agreement with the value of T_c determined from the $C(T)$ peak. This means that **1** is AF-ordered below T_c due to the strong FM exchange interaction along the chains and a weaker AF interaction between the chains. In general, the magnetic susceptibility of the anisotropic, ferromagnetic spin chain is expected to follow the dependence $\chi T = C_{\text{eff}} \exp(-\Delta_\xi/k_B T)$ in the low-temperature limit. The parameter Δ_ξ represents the energy of the domain wall in the spin chain, k_B is the Boltzmann constant, and C_{eff} is an effective Curie constant. In the Ising chain model, $\Delta_\xi = J_{\text{Ising}}/2$. The plot of $\ln(\chi T)$ versus $1/T$ (Figure 3) shows that this dependence is linear in the range from 6 to 15 K, but at lower temperature the interchain AF interaction causes a deviation. For a quantitative analysis, the Ising model as used for the specific heat data analysis is applied, including the interchain interaction, J' , with z neighboring chains in the molecular field approximation and the Zeeman term that depends on the g -factors of the ground $s = 1/2$ state. The equations are the same as those given in ref. [7]. The parameters obtained by using the 100 Oe data from 5 to 10 K are $g_z = 6.87(6)$, $J_{\text{Ising}} = 21.9(2)$ cm⁻¹, and $zJ' = -0.27(1)$ cm⁻¹. The perpendicular $g_x = g_y = 2.5$ are fixed in this analysis to reduce the number of free parameters and to match the expected approximate relation between g_z and g_x for the ground state of an axially distorted octahedral cobalt(II).^[13]

An external field higher than the critical field, H_c , overcomes the AF interaction between the chains, leading to a metamagnetic transition (MT), which is demonstrated by the experimental magnetization, $M(H)$, measured below T_c (see Figures S27 and S28 in the Supporting Information). The $H_c(T)$ phase diagram is presented in Figure S29. Powder samples were used for all the measurements, and therefore H_c is determined as

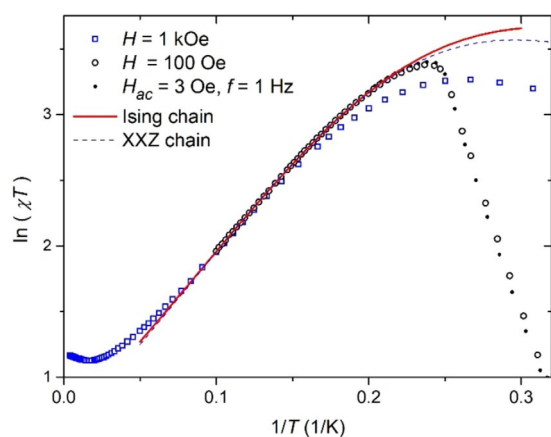


Figure 3. Low-temperature magnetic susceptibility of **1** analyzed by using the Ising chain model (red line) and the XXZ model (dashed line).

the field at which d^2M/dH^2 is maximal, that is, at the $M(H)$ knee. At this field, crystallites that are oriented with their easy axis along the applied magnetic field start to undergo the MT. The grains tilted away from this alignment require a higher field. Another effect that flattens the $M(H)$ step is the demagnetization field due to the FM (saturated paramagnetic) phase (see the Monte Carlo simulations below). For **1** in the range from 1.9 to 3.2 K, the value of H_c is 292(3) Oe.

Monte Carlo simulations of the magnetic structure

To better understand the influence of the magnetic field on the relaxation properties of AF-ordered FM chains in such compounds, we present simulations of the ground-state magnetic structure of **1** and of its behavior during the MT. The following assumptions were used. 1) The moments are arranged as in the structure of **1**, truncated to a spherical grain of diameter 30 nm, which corresponds to 32 000 moments creating 920 chains. 2) The Ising anisotropy of strong, FM intrachain interactions aligns all the moments in one chain along the Co–N_{py} bonds, within one chain all in the same direction, leaving only two possible states for every chain in the simulations. The value of each moment is $g_z S \mu_B$ with $g_z = 7.0$ (μ_B = the Bohr magneton). 3) The total energy includes the interchain exchange, dipole–dipole, and Zeeman terms, and was minimized by using the Monte Carlo Metropolis algorithm. 4) The dipole–dipole interaction energy is calculated for every pair of moments from different chains. The dipole–dipole interactions for moments within the same chain are not included, because this energy is effectively included in the intrachain interaction, J_{isng} , and in assumption (2) above. 5) The interchain exchange interaction, $-J_{2S_1S_2}$, is present only for such pairs of cobalt(II) moments for which C–H...O as well as C–H...S contacts, marked in Figure S24 in the Supporting Information, can mediate weak magnetic exchange. In this way, each cobalt has two nearest neighbors from other chains. 6) The external field is applied along the average easy axis of the two crystallographic Co1 and Co2 positions. It is also verified that the postulated average easy axis that is used in the Monte Carlo simulations dif-

fers by only 2.6° from the easy axis determined for the Co1...Co2 dimer based on ab initio calculations (see below).

The only optimized parameter is J_2 , and the value $J_2 = -0.15 \text{ cm}^{-1}$ reproduces the AF ground state with $H_c = 290 \text{ Oe}$, as observed experimentally for **1**. The major results of these simulations are shown in Figure 4 and Figure S30 in the Supporting Information. The exchange interaction, J_2 , is essential to obtain a MT; this would not be possible with dipolar interactions only, for any given orientation of the axis of anisotropy. Moreover, the dipolar field at the cobalt sites, produced by the remaining chains in the AF-ordered state for the assumed anisotropy axis, is about $H_{\text{dip}} = +74 \text{ Oe}$, slightly different for the two cobalt sites. Its positive sign means that H_{dip} alone would produce an FM ground state with magnetic domains (see Figure S30). Thus, H_{dip} effectively decreases the influence of J_2 .

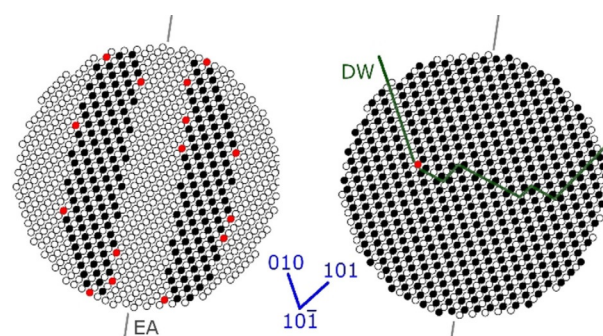


Figure 4. Magnetic structures obtained by Monte Carlo simulations of the magnetic moments in **1**. The view is along the $10\bar{1}$ axis, that is, along the cobalt chains. Each dot denotes a single chain of spins, black and white points denote the two possible magnetization directions along the easy axis (EA), and red points denote all the chains that are flipped when H is increased by an additional 20 Oe. Left: The MT with AF and FM regions in the field $H = 400 \text{ Oe}$ along the EA. Right: AF state at $H = 0$, but with a defect: the domain wall (DW) between 3D domains.

For each chain in the ordered AF structure, the MT occurs when the external field compensates the molecular field of the exchange interaction and dipolar fields along the easy axis, that is, in our case, in the H range from $H_c = 290$ to about 500 Oe (see Figure S31 in the Supporting Information). $M(H)$ changes gradually, even for a monocrystalline grain and even for the field aligned with the easy axis, due to demagnetization. For grains other than spherical ones, the upper limit would change, up to about 600 Oe for needle-shaped grains, which are typical in powder samples of **1**.

The most important conclusion concerns the identification of chains that can be flipped by a small H_{ac} field, a situation that is possible when the molecular exchange field, dipolar field, and the external field compensate to almost zero. The chains that are flipped by an additional increase in field of 20 Oe are marked in red in Figure 4. The ac susceptibility signal originates mainly from these types of chains. At a field in the range of the MT (e.g., 400 Oe), they are numerous, as they exist at every border between the AF and FM regions, which is where the FM regions gradually grow at the expense of the AF regions, when the field increases (Figure 4, left).

However, at $H=0$, in the perfect AF-ordered system at $T=0$ K (see Figure S32), there are no chains that can flip in response to a small field change. Only some defects in the magnetic structure allow for their existence, because the cancellation of the long-range dipolar field to zero requires an inversion-like symmetry of the nearest and farther spin neighbors, which is uncommon. The small number of such chains at zero field (Figure 4, right) corresponds to a much smaller ac susceptibility relaxation amplitude measured at zero H (see Figure S32). These MC simulations suggest that magnetic relaxations at $H=0$ in such AF-ordered $[\text{Co}(\text{NCS})_2(\text{L})_2]$ chains in the low-temperature limit originate mainly from such defects.

The second source of ac susceptibility and its magnetic relaxation at $H=0$ is the presence of thermal excitations of chains or magnons in the three-dimensional AF magnetic structure, which is not considered in the above MC simulations. At temperatures much lower than T_c , such thermal excitations can be neglected, but close to T_c , their influence may become dominant in the ac susceptibility at $H=0$.

Dynamic magnetic properties of pristine and defect samples

The ac magnetic measurements on pristine samples of **1** in the AF-ordered phase below T_c are hindered by its very small ac susceptibility. This can be technically overcome by applying a bias magnetic field, H , to bring the system into the range of the MT and facilitate the flipping of spin chains, even by small H_{ac} fields. However, questions arise as to how the magnetic field influences the magnetic relaxation time, τ , and whether the determined energy barrier of chain reversal, Δ_{τ} , remains unchanged. To answer these questions, we performed systematic ac susceptibility versus frequency measurements over a range of external fields and temperatures. The ac data were analyzed by using the single-mode Cole–Cole model. The results are presented in Figure 5 with the fitted ac susceptibility curves shown in Figure S33 in the Supporting Information (see also Table S4). As predicted by our MC simulations, the data for polycrystalline samples measured in an applied field deviate

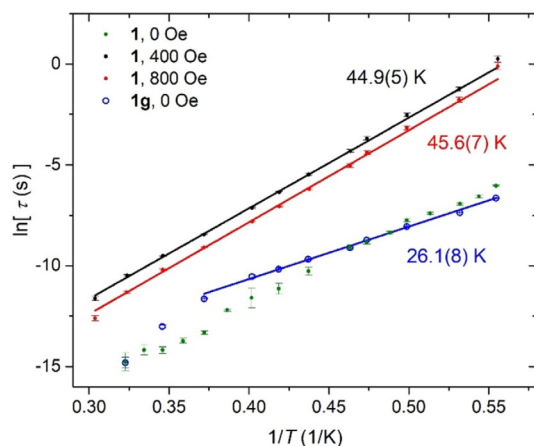


Figure 5. Temperature dependence of the relaxation time obtained by using single-mode Cole–Cole analysis of the ac susceptibility of **1**, measured at different applied dc magnetic fields, and for the ground sample **1g**.

from the single-mode Cole–Cole model, because some of the grains are below the MT, some are above, and some are in the MT range. For example, by using the data measured at 1.85 K across the whole of the measured frequency range 0.1–1500 Hz, the distribution parameter, α , of the Cole–Cole model lies between 0.49 and 0.62 at 400 and 800 Oe, respectively. This means that the obtained relaxation time, τ , represents an average of a wide distribution of relaxation times. Nonetheless, the $\ln\tau(1/T)$ dependence is linear. The Arrhenius energy barrier determined for pristine samples of **1** is $\Delta_{\tau_1}=44.9(5)$ K using the data measured at 400 Oe in the temperature range 1.8–3.2 K, and a very similar value is obtained at 800 Oe.

The analysis of similar measurements at $H=0$ creates two problems: The ac susceptibility (see Figures S34 and S35 in the Supporting Information) is very small and depends on the sample batch. The data for **1** at $H=0$ are very similar to those previously reported,^[9] when it was fitted with the Arrhenius law with a single energy barrier of 38.4 K, in spite of the visible curvature of the $\ln\tau(1/T)$ dependence. In general, a crossover temperature, T^* , is expected for SCMs due to the finite size of the relaxing chains.^[1a] However, for **1** at $H=0$, the available temperature range above 1.8 K does not allow us to determine the energy barrier below T^* .

To circumvent these problems, we used a sample ground in a hand mortar (denoted as **1g**) with the aim to create more crystal structure defects to facilitate the creation of AF domain walls in the ordered state and to increase the ac susceptibility at $H=0$. The ac susceptibility of **1g** is indeed much greater than that of **1** (see Figure S34 in the Supporting Information), which makes further analysis more convincing. The fitted relaxation times are included in Figure 5. The grinding shifts T^* to a higher temperature, 2.6 K, and facilitates the determination of the relaxation barrier below T^* , with $\Delta_{\tau_2}=26.1(8)$ K being obtained. The value of T^* corresponds to an average chain length $n = \exp(J_{\text{sing}}/2k_B T^*)/2$ of about 200 cobalt units, for chains that add up to give the ac susceptibility of the **1g** sample at $H=0$. For sample **1**, an estimated $T^* < 1.9$ K for the majority of chains corresponds to $n > 2000$ cobalt units. Therefore, grinding of such samples seems to be an easy method to shift the crossover temperature, such that the Δ_{τ_2} barrier can be determined precisely.

Field dependence of the ac relaxations

The field dependence of the magnetic relaxation times of **1** is shown in Figure 6 for two temperatures at which the data from the available frequency window 0.1–1500 Hz allows us to convincingly determine τ in the whole field range 0–800 Oe. The susceptibility χ' (χ'') plots, including fitted curves, are shown in Figures S35 and S36 in the Supporting Information. Around $H=H_c$, the relaxation time, τ , of the main ac susceptibility component suddenly changes between 300 and 200 Oe, by a factor of 800 at 1.85 K and by a factor of 230 at 2.4 K. This clearly points to two different relaxation processes, labeled A and B in Figure 6. A comparison with the $\ln\tau(1/T)$ data in Figure 5 allows us to identify process A as being related to short chains created by defects, whereas process B is related

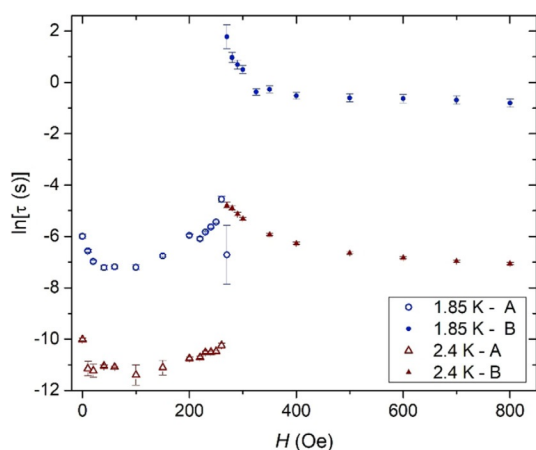


Figure 6. Field dependence of the magnetic relaxation time of **1**, measured at 1.85 and 2.4 K. Open symbols denote relaxation times identified as related to short chains, solid symbols denote relaxation times of long chains.

to much longer chains, which effectively exhibit a higher energy barrier down to 1.8 K and longer relaxation times.

The $\tau(H)$ dependence of an SCM has been investigated, for example, for a monocrystal sample of Mn_2Ni , which was described as an AF phase of SCMs.^[14] It was also numerically simulated by using various probability laws.^[15] In the simplest case of a Glauber-type relaxation for an isolated infinite Ising chain, $\tau(H) = \tau_{H=0}/(1 + x^2/2)$, in which $x = (g\mu_B H/k_B T) \exp(2J_{zz}s^2/k_B T)$. This model predicts a maximum $\tau(H)$ at zero field and its decrease in an applied field.

However, for AF-coupled and -ordered chains as in **1**, H in the above equation should be exchanged by the sum of the molecular field, H_{mol} , and the external field, H . In such a case, the maximum of the measured $\tau(H)$ should be at H_c , because then H_{mol} is compensated by H for one sublattice of AF-ordered spins, at least for crystallites having the easy z axis along H . The data in Figure 6 show a maximum at 270 Oe, which is slightly lower than $H_c = 290$ Oe, but the $\tau(H)$ dependence does not fit at all. The main reason for this is that below H_c the measured τ represents short chains, whereas above H_c the measured τ represents long chains. The second reason is the fact that the sample is polycrystalline, and for crystallites with the angle θ between H and the easy axis, compensation occurs when $H \cos \theta = H_c$. The distribution of θ leads to a wide distribution of relaxation times, which is indeed observed experimentally. This makes an exact analysis of the whole $\tau(H)$ dependence practically impossible.

Computational studies

Theoretical studies based on DFT and ab initio calculations were performed on **1** to gain further insights in its magnetochemistry (see also the Computational details in the Experimental Section).

The anisotropy of the single ions was calculated at the CASSCF/CASPT2/RASSI-SO level for the two crystallographically independent cobalt(II) (Co1 and Co2), based on the corresponding mononuclear cobalt(II) structural models **1-Co1** and

1-Co2, respectively (see Figure S37 in the Supporting Information). The main difference between the two octahedrally coordinated centers can be attributed to the orientation of the two apical 4-methoxypyridine co-ligands with respect to the thiocyanate chain direction (Co1: perpendicular/perpendicular; Co2: parallel/parallel). Continuous shape measures indicate a slight deviation from the ideal octahedral coordination geometry for both cobalt centers (Co1: $S(O_h) = 1.110$; Co2: $S(O_h) = 1.113$; ideal octahedron: $S(O_h) = 0$ with an upper limit of 100).^[15] Nevertheless, this distortion leads to a notable splitting of the ${}^4T_{1g}({}^4F)$ ground-state multiplet for both spin centers (relative CASPT2 energies: 1233 cm^{-1} (**1-Co1**) and 1052 cm^{-1} (**1-Co2**); see Table S5). In the case of cobalt(II), dynamic electron–electron correlation needs to be taken into account, that is, by performing additional CASPT2 calculations to adequately describe their magnetic properties. The importance of the latter can be seen from the significant energy shift of approximately 2700 cm^{-1} in the case of the lowest doublet state of **1-Co1** and **1-Co2** upon including a dynamic correlation with CASPT2 (relative energy of the lowest doublet state: 9301 (**1-Co1**) and 8887 cm^{-1} (**1-Co2**)). Moreover, the splitting of the ${}^4T_{1g}({}^4F)$ ground-state multiplet is further increased by the additional inclusion of spin–orbit coupling (**1-Co1**: 1637 cm^{-1} ; **1-Co2**: 1508 cm^{-1} ; see Table S6). At the same time, the spin–orbit coupling leads to an isolated ground-state KD for both centers (**1-Co1**: $E_{KD2} = 130\text{ cm}^{-1}$; **1-Co2**: $E_{KD2} = 155\text{ cm}^{-1}$). Consequently, this justifies the use of an $s = S_{\text{eff}} = 1/2$ effective spin Hamiltonian for the interpretation of the magnetic properties of **1** at lower temperatures.

The calculated Cartesian components of the g tensor for the first two KDs in **1-Co1** and **1-Co2** are given in Table 2. For both paramagnetic centers, an easy axis of magnetization, g_z , with $g_z \gg g_x, g_y$ within the ground-state KD was obtained. The ground-state KD g_z value of 7.004 in **1-Co1** is slightly higher than the corresponding one in **1-Co2** with a value of 6.568. The average of both g_z values (6.786) is in good agreement with the experimental value of 6.87(6) obtained from fitting the static magnetic susceptibility data at 100 Oe (see above). In a previous study,^[6a] we reported that the perpendicular/perpendicular orientation of the π planes of the pyridine-based co-ligands with respect to the direction of the thiocyanate chain leads to higher single-ion anisotropy than a parallel/parallel orientation. This trend is confirmed by the ab initio calculations for **1-Co1**

Table 2. Main components of the g tensor ($S_{\text{eff}} = 1/2$) and relative energies for the first two Kramers doublets (KDs) of **1-Co1** and **1-Co2**, respectively, obtained from ab initio calculations (CASSCF/CASPT2/RASSI-SO).

		1-Co1	1-Co2
KD1	$E_{KD1} [\text{cm}^{-1}]$	0	0
	g_x	1.840	2.017
	g_y	3.017	3.734
	g_z	7.004	6.568
KD2	$E_{KD2} [\text{cm}^{-1}]$	130	155
	g_x	1.627	1.182
	g_y	1.892	1.366
	g_z	5.664	5.608

and **1-Co2** presented in this work. Furthermore, transversal components of the g tensor, g_x and g_y , are apparent for both centers, which indicates a non-ideal Ising anisotropy. The magnetic axes of the ground-state KD for an effective spin $S_{\text{eff}} = 1/2$ are depicted in Figure 7 and show that the easy axis of mag-

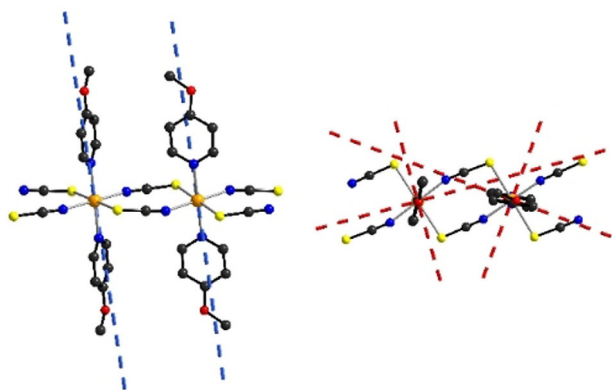


Figure 7. Representation of the magnetic axes of the ground-state Kramers doublet ($S_{\text{eff}} = 1/2$) obtained from ab initio calculations on **1-Co1** and **1-Co2**, projected onto a dinuclear cobalt(II) chain fragment (blue dashed lines: g_z ; red dashed lines: g_x and g_y). Left: Complete fragment (hydrogen atoms have been omitted for clarity). Right: View along the Co–N_{py} axes. The angle between the two g_z axes is 10.0° .

netization, g_z , for both centers is nearly parallel to the Co–N_{pyridine} bond vectors (angle between both vectors: 10.0° (**1-Co1**) and 7.8° (**1-Co2**)). This finding supports the assumption regarding the orientation of the magnetic moments within the Monte Carlo simulations performed on the bulk material. The angle between both easy axes of magnetization was found to be 10.0° , which shows a deviation from ideal Ising behavior that assumes a parallel alignment of the spins. The corresponding hard plane of magnetization, given by the g_x and g_y magnetic axes, was found to be within the [N₂S₂] coordination plane of the thiocyanate ligands (angle between planes: 10.6° (**1-Co1**) and 8.3° (**1-Co2**)). The first excited KDs in **1-Co1** and **1-Co2** also show an easy axis of magnetization, however, the orientation of these axes is within the [N₂S₂] coordination plane formed by the thiocyanate ligands. The orientation of the latter seems to be directed by the orientation of the 4-methoxypyridine π planes (angle between the π plane and easy axis: 20.2° (**1-Co1**) and 5.6° (**1-Co2**); angle between both easy axes: 68.5°).

The magnetic intrachain exchange in **1** was studied by broken-symmetry DFT (BS-DFT) calculations (see also the Computational details in the Experimental Section). For these calculations, a dinuclear model was employed (denoted as **1-Co1Co2** and depicted in Figure S38 in the Supporting Information) to investigate the magnetic exchange interaction between the two crystallographically independent Co1 and Co2. The calculated coupling constant of $J_{12} = 10.1 \text{ cm}^{-1}$ confirms FM intrachain coupling (see Table S7 for details), which is in accordance with experiment. It is important to note that the coupling constant J_{12} , as obtained by BS-DFT calculations, does not represent the experimental coupling constants, because both

are based on different representations of spin Hamiltonians (J_{12} represents the isotropic Heisenberg interaction of spin $S = 3/2$ and J_{Ising} corresponds to the Ising interaction of spin $s = 1/2$). Nevertheless, the BS-DFT calculations performed on the dinuclear model **1-Co1Co2** help to qualitatively confirm the type of intrachain magnetic exchange in the 1D periodic chain **1**. The corresponding spin density plots for the high-spin and broken-symmetry states are visualized in Figure S39. In both states, most of the spin density is localized at the central cobalt ions, and only a weak spin polarization of the neighboring nitrogen donor atoms is observed.

FD-FT THz-EPR measurements

EPR spectroscopy can be employed to probe magnetic excitations in SCMs, and has the great advantage over other methods that energy gaps and also g values can be determined directly and with high precision as well as accuracy without the need to make any assumptions as to the coupling model of the chains. Field-domain EPR has already been applied to a number of SCMs,^[3d,6a,16] including a cobalt(II)-based, μ_2 -Cl-bridged, 1D spin chain with pyridine-based co-ligands,^[16b] similar to **1**, and the very closely related compound [Co(NCS)₂(py)₂]_n.^[6a] Frequency-domain EPR has also been used in the study of [CoCl₂(py)₂]_n.^[17] The advantages of frequency- over field-domain EPR spectroscopy for the investigation of SCMs are the possibility of measuring zero-field spectra as well as larger EPR transition energies that are accessible by using broadband sources, and the comparability of the absorption intensities over the entire excitation energy range.

We recorded field-dependent, low-temperature (5 K) FD-FT THz-EPR spectra of a pressed powder sample of **1** up to 7.5 T. The spectra are presented in Figure 8 in the form of magnetic-field division spectra (MDS) to remove signals from nonmagnetic transitions and show resonances at lower fields as upward pointing peaks and those at higher fields as downward pointing peaks. The field-independent line at 41.5 cm^{-1} (*) is an artifact resulting from zero transmission due to a very intense vibrational transition. The oscillatory baseline in the 1 T/0 T spectrum is due to Fabry–Pérot interferences, probably induced by a tiny displacement of the sample in the B_0 field. At zero field (MDS 1 T/0 T), the energy gap between the ground and the first excited state of the SCM can be directly determined to be $\Delta_{\text{EPR}} \approx 19.0 \text{ cm}^{-1}$. A g -factor corresponding to $g_z \approx 6.8$ can be extracted from the most prominent shift of the signal to higher energies with increasing field B_0 , illustrated by the green solid line. This value is in good agreement with the value obtained from the static magnetic susceptibility at 100 Oe (6.87(6)) and also with the average of the ground-state KD g_z values of **1-Co1** and **1-Co2** determined from the ab initio calculations (6.786). Furthermore, the spectra show no EPR transitions with field-dependent shifts by multiples of this g value, which indicates that the observed magnetic excitations are due to localized single-spin reversals (number of flipped spins $m = 1$) rather than spin-cluster excitations ($m > 1$),^[17,18] which are not detected. These latter transitions would gain intensity if there were significant transverse components

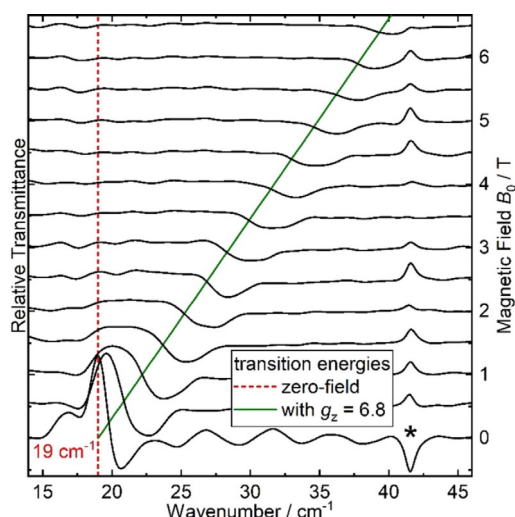


Figure 8. Field dependence of the FD-FT THz-EPR spectra of **1** measured at 5 K with a resolution of 1 cm^{-1} using an Hg arc lamp. In the relative transmittance MDS (black solid lines), obtained by division of a raw spectrum at $B_0 + 1\text{ T}$ by one measured at B_0 , the maxima correspond to stronger absorption at lower B_0 , the minima to increased absorption at higher B_0 .

of the intrachain exchange interaction (J_{xx} , J_{yy}), leading to mixing of different Ising states (Ising–Heisenberg chain). These results again validate the applied Ising chain model, including interchain interactions and the obtained spin Hamiltonian parameters for **1**. It is noted that the signals shown in Figure 8 do not represent transitions between the ground and first excited Kramers doublets of the individual cobalt(II) centers, which would be expected at around $130\text{--}155\text{ cm}^{-1}$ according to calculations.

The temperature dependence of the magnetic excitations has also been investigated, and zero-field spectra are shown in Figure 9. Because, in contrast to MDS, the positions of the peak maxima are not biased by spectral contributions at another field, the EPR transition energies can be determined even more accurately. A shift of 0.1 cm^{-1} from 19.2 cm^{-1} at 2.4 K to 19.1 cm^{-1} at higher temperatures ($\geq 4.6\text{ K}$) is observed. This can be rationalized by the AF magnetic ordering of the chains, which means that additional energy is required for the excited spin to overcome the interchain interaction below the critical temperature T_c . In a recent FD-FT THz-EPR study on mononuclear high-spin cobalt(I) clathrochelate complexes, a similar phenomenon was observed in the form of an increase of the zero-field resonance energy with temperature.^[19] It was interpreted in terms of weak AF interactions, however, between single molecules instead of 1D chains.

For **1**, the temperature range in which the shift occurs is consistent with $T_c = 3.94(1)\text{ K}$ determined from the specific heat data. If the shift is indeed a result of AF ordering, it should not be present at fields above H_c , in which the chains are effectively decoupled from each other. The temperature dependence of 1 T/0 T MDS, presented in Figure S41 in the Supporting Information, illustrate that this is the case. Whereas the 0 T peaks, pointing upwards, exhibit a shift of 0.1 cm^{-1} between 2.2 and 4.7 T, the 1 T peaks, pointing downwards, do not. The

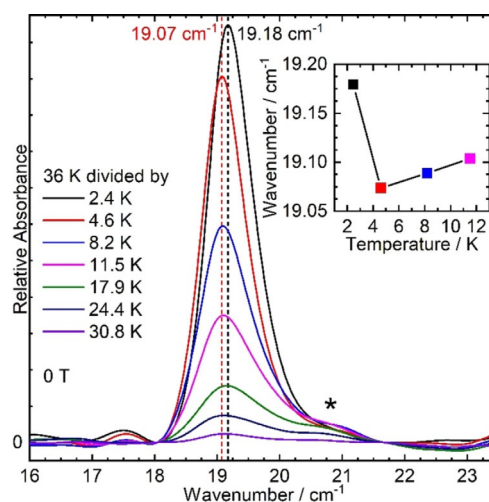


Figure 9. Temperature dependence of the zero-field FD-FT THz-EPR signal of **1**, measured with a resolution of 0.5 cm^{-1} using low- α mode coherent synchrotron radiation, and presented as relative absorbance (temperature division spectra). Inset: Zero-field EPR transition energies, that is, the energy gap between the ground and first excited states, at the four lowest temperatures measured. With increasing temperatures, the apparent peak maximum is shifted to slightly higher wavenumbers, as a non-magnetic, vibrational transition at around 20.8 cm^{-1} (*) becomes more dominant, and possibly due to temperature-dependent structural changes in the crystallite lattice.

critical field of the MT derived from dc magnetic measurements, $H_c = 292\text{ Oe}$, corresponds very precisely ($2g_d\mu_B sH_c = 0.093\text{ cm}^{-1}$) to the observed shift of 0.1 cm^{-1} , which represents the energy of the interchain couplings along the easy axis for a spin system with $g_z \approx 6.8$. Finally, it is noted that the energy gap $\Delta_{\text{EPR}} = 19.1\text{ cm}^{-1}$ in the magnetically disordered phase is of a comparable size to $J_{\text{Ising}} = 21.9\text{ cm}^{-1}$ determined from specific heat and dc magnetic measurements, albeit somewhat smaller. This difference is discussed in the following.

Discussion within XXZ and XYZ spin chain models

The above analysis of specific heat and susceptibility, similar to all previously reported $\text{Co}(\text{NCS})_2$ chains, relied on the Ising model [Eq. (1)], mainly due to its simplicity. In this section, we provide a quantitative rationale, also presenting an attempt to go beyond the Ising model. Using the ab initio calculated wave functions of all 12 states within the $^4T_{1g}$ ground-state multiplet, we calculate the exchange Hamiltonian for the dimer built of **1-Co1** and **1-Co2** (denoted below as **1-Co1...1-Co2**) by using the Lines model^[20] with the help of the POLY_ANISO program of the Molcas package.^[21] The four lowest energy levels calculated for test values of the isotropic exchange, J_{Lines} (see Figure S42 in the Supporting Information), can be equated to eigenvalues of the Hamiltonian for the dimer with $s = 1/2$ spins according to Equations (2) and (3):

$$\hat{H}_2 = -J_{xx}S_1^xS_2^x - J_{yy}S_1^yS_2^y - J_{zz}S_1^zS_2^z \quad (2)$$

$$\begin{pmatrix} E_1 \\ E_2 \\ E_3 \\ E_4 \end{pmatrix} = \frac{1}{4} \begin{pmatrix} 1 & -1 & -1 \\ -1 & 1 & -1 \\ -1 & -1 & 1 \\ 1 & 1 & 1 \end{pmatrix} \begin{pmatrix} J_{xx} \\ J_{yy} \\ J_{zz} \end{pmatrix} \quad (3)$$

This is possible because the isotropic exchange J_{Lines} is a perturbation that splits the ground, four-fold degenerated state of the dimer. For **1-Co1...1-Co2**, the next states have energies at least 130 cm^{-1} higher (see Table 2). Therefore, the $E_i(J_{\text{Lines}})$ dependence is almost linear. The values $J_{zz}/J_{\text{Lines}} = 5.950$, $J_{yy}/J_{\text{Lines}} = \pm 1.479$, and $J_{xx}/J_{\text{Lines}} = \pm 0.988$ are obtained, but the common sign of J_{xx} and J_{yy} cannot be determined in this way due to possible permutations of E_i . However, this sign is not important for further analysis of data at zero field. The J_{ii} parameters obtained for the dimer can be directly applied to the chain Hamiltonian given by Equation (4):

$$\hat{H} = - \sum_i (J_{xx} S_i^x S_{i+1}^x + J_{yy} S_i^y S_{i+1}^y + J_{zz} S_i^z S_{i+1}^z) \quad (4)$$

because the orientation of the main axes of exchange, J_{ii} , is the same for every Co1...Co2 pair in the chain of 1.

The calculated anisotropy (J_{xx}/J_{zz} and J_{yy}/J_{zz} values) of the effective exchange Hamiltonian [Eq. (4)] can be tested against the specific heat data shown in Figure 2 to obtain the energy scale, for example, J_{zz} . To simplify the calculations and to reduce the number of fitted parameters, we partly restrict our further analysis to a simpler case with $J_{xx} = J_{yy} \neq J_{zz}$, that is, to the XXZ model. As limiting cases, the XXZ model includes the Ising model for $J_{xx} = 0$, the Heisenberg model for $J_{xx} = J_{zz}$, the XY model for $J_{zz} = 0$, and all the cases in between, which allows for a wide range of quantum phenomena. For very short chains such a model was studied, for example, by Bonner and Fisher,^[22] and limited quantities can be calculated for infinite chains by using the Bethe ansatz approximation.^[23] Here, to calculate specific heat and elementary excitations of such infinite XXZ spin chains, we used an algorithm based on the density renormalization matrix group (DMRG), which provides a state-of-the-art toolbox for simulations of quantum systems in one dimension (see ref. [24] for a review). Figure 10 shows the evolution of the specific heat of the XXZ chain from the FM Ising chain for $J_{zz} > 0$, $J_{xx} = 0$, through the isotropic FM Heisenberg chain that becomes critical at $T = 0$, through the XY model for $J_{zz} = 0$, to the AF Heisenberg chain, and back to the Ising chain, this time AF. This specific heat does not depend on the common sign of J_{xx} and J_{yy} because of the symmetry of changing the sign of x and y axes for every second spin.

Fitting J_{xx}/J_{zz} and J_{zz} parameters to the specific heat data of **1** (Figure 2), together with the lattice contribution, we obtain $J_{xx}/J_{zz} = 0.22(15)$ and $J_{zz} = 22(3) \text{ cm}^{-1}$, in agreement with the predicted anisotropy $(J_{xx} + J_{yy})/(2J_{zz}) = 0.207$, but with large uncertainties. For this reason, it is better to use the energy gap Δ_{EPR} precisely determined by EPR spectroscopy, which allows the energy scale of the spin Hamiltonian given by Equation (4) to be established.

In this approach, it is necessary to calculate the excitations from the ground state of such an XXZ chain. For the ferromag-

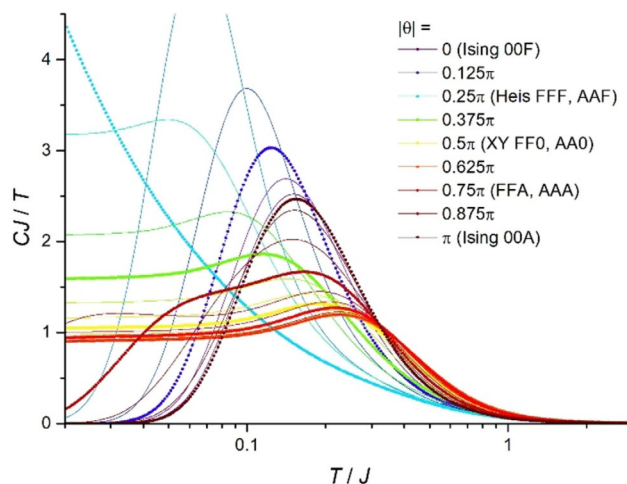


Figure 10. Specific heat of the $S = 1/2$ XXZ chain, calculated by using the DMRG technique for equidistant values of $\theta = \arctan(J_{xx}/J_{zz})$. The scale of the axes is determined by $J = (J_{xx}^2 + J_{zz}^2)^{1/2}$.

netic and dominant $J_{zz} > |J_{xx}|$, the energy of the spin chain excitation was calculated by using the Bethe ansatz (BA).^[23] For a closed ring, the string solution that consists of m consecutive spins down and remaining spins up has the energy E , relative to the ground state, depending on the wave vector K given by Equation (5)

$$E(K) = 2mh + |J_{xx}| \sinh \phi \frac{\cosh m\phi - \cos Ka}{\sinh m\phi} \quad (5)$$

in which $\cosh \phi = J_{zz}/J_{xx}$, $h = g\mu_B S H_z$, and $J_{zz} > |J_{xx}| > 0$. The $E(K)$ dependence for **1**, that is, for $J_{xx}/J_{zz} = 0.207$, is shown in Figure 11.

Thermal excitations (phonons) have the same range of lattice momentum as magnons, so magnons in the whole K range, from $-\pi/a$ to $+\pi/a$, can be thermally excited (a is the Co...Co distance). The ac susceptibility measurements probe mainly excitations with high m , because the measured ac magnetization is proportional to m . According to Equation (5), the energy E becomes practically independent of K for $m = 5$, and for high m saturates at a value given by Equation (6),

$$E = \sqrt{J_{zz}^2 - J_{xx}^2} + 2mh \quad (6)$$

that is, $0.978J_{zz}$ for **1**, which is almost the same as for the Ising model. The single domain wall energy, which is obtained from the dc susceptibility analysis, is $\Delta_\xi = 0.978J_{zz}/2$. This solution is not contained directly in Equation (5) because of imposed closed-ring boundary conditions. In EPR spectroscopy, only magnons with $K < 10^{-6}\pi/a$ can be excited by 19 cm^{-1} photons, due to the conservation of lattice momentum. If only one spin can be flipped, that is, $m = 1$, the energy of the created magnons is given by Equation (7).

$$\Delta_{\text{EPR}} = E_{K=0, m=1} = J_{zz} - |J_{xx}| + 2h \quad (7)$$

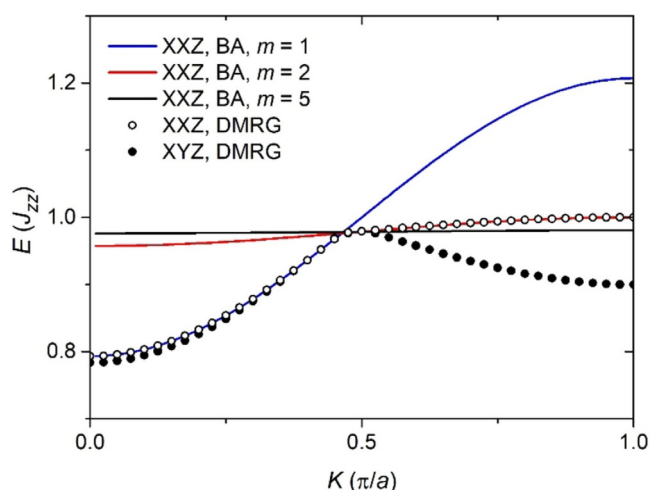


Figure 11. Simulated low-energy excitations of **1** obtained by using the Bethe ansatz for the XXZ model (BA, lines) and the DMRG technique for the XXZ (open points) and XYZ models (solid points).

The anisotropy of the exchange interaction, $J_{xx}/J_{zz}=0.21$, as estimated from the ab initio wave functions of the **1-Co1...1-Co2** dimer, and $J_{zz}-J_{xx}=19.1\text{ cm}^{-1}$, derived by EPR spectroscopy for $h=0$, lead to the spin Hamiltonian parameters $J_{zz}=24.08\text{ cm}^{-1}$ and $J_{xx}=5.00\text{ cm}^{-1}$.

The excitation for $m=2$ would have the energy given by Equation (8),

$$E_{K=0,m=2} = J_{zz} - J_{xx}^2/J_{zz} + 4h \quad (8)$$

which is 23.0 cm^{-1} for the above-determined exchange parameters, however, such a transition is not visible in Figure 9.

To estimate the errors introduced by the simplification of the XYZ model to the XXZ model, a similar calculation of the energy excitations can be made for XYZ, however, the BA solution is cumbersome in this case. Therefore, we present here the lowest excitation energy for the XYZ model obtained by the DMRG technique. Discrete points in Figure 11 show the dispersion relation calculated by using the variational uMPS excitation ansatz.^[24c,25] The results obtained for the XXZ model ($J_{xx}/J_{zz}=0.207$) are in perfect agreement with the BA, which is a good test of our implementation of this algorithm. A similar calculation for the full XYZ model ($J_{xx}/J_{zz}=0.166$, $J_{yy}/J_{zz}=0.248$) leads to a very similar $E(K=0)$ value. However, a new type of lowest-energy excitation is present for $K > 0.5\pi/a$. A comparison of $E(K)$ with the XYZ model BA solutions suggests that it is the lowest branch of the spinon solution that is present for AF $s=1/2$ chains, but also for FM XYZ chain models.^[23] Such excitations, invisible in EPR spectroscopy, influence slightly the specific heat and susceptibility.

The J_{zz} and J_{xx} parameters obtained from EPR data reproduce reasonably the specific heat data (see Figure S43 in the Supporting Information). It was also verified that the Schottky anomaly related to excited cobalt(II) states is negligible for the analysis of the specific heat presented above. Similarly, the susceptibility $\ln(\chi T)(1/T)$ curve is reproduced with the same J_{zz} and J_{xx} parameters by adjusting only two parameters, $g_z=$

$6.59(1)$ and $zJ' = -0.27(1)\text{ cm}^{-1}$, defined identically as in the analysis above, using the Ising model (Figure 3). The powder susceptibility is calculated to be $(2\chi_x + \chi_z)/3$ by using the χ_x and χ_z susceptibilities for the infinite XXZ Heisenberg spin chain. The temperature dependence of the susceptibility cannot be obtained by using the BA approach in this case, but by using the DMRG technique an arbitrary direction of the applied field can be accounted for (see Figure S44).

Finally, the energy barriers of ac relaxations, Δ_{r1} and Δ_{r2} , should differ by the energy of the single domain wall, Δ_ξ . Using data from Figure 5 for $1/T$ above 0.4 K^{-1} , $\Delta_{r1} - \Delta_{r2} = 13(1)\text{ cm}^{-1}$. For comparison, the XXZ model provides $\Delta_\xi = 11.7\text{ cm}^{-1}$, which is very close.

Conclusions

The present work is part of a much larger project on the magnetic properties of Co(NCS)_2 chain compounds with different pyridine derivatives as co-ligands that show single chain relaxations in the AF phase and a metamagnetic transition at critical fields dependent, for example, on the nature of the co-ligands. Considerable effort was devoted to these previous investigations, but important questions remained. Therefore, compound **1** was selected as a model compound and investigated in detail by a combination of sophisticated experimental and theoretical methods that go far beyond what has previously been applied to this class of SCMs, including investigations of the influence of the magnetic field on the relaxation properties especially in the AF-ordered state, performed by Monte Carlo simulations that are based on the ab initio calculated single-ion anisotropy. The results clearly show that inter-chain interactions, which are responsible for the AF ordering, cannot be explained by only dipolar interactions, because they are ferromagnetic and therefore also exchange coupling is essential. In this context, it is noted that the critical field of the metamagnetic transition can also be detected by EPR spectroscopy, in which a small shift of the spin excitation energy is observed. Much more importantly, Monte Carlo simulations show that both the molecular interchain exchange and external fields have a huge impact on the ac magnetic relaxations, because only chains located at specific sites in the magnetic domain walls can flip in small ac fields, because the cancellation of both dipolar and exchange fields is required for such chains. This means that the ac susceptibility signal measured at zero field mainly depends on the number of defects, which was experimentally confirmed by comparing the experimental data for pristine and ground samples. The grinding increases the susceptibility and also shortens the chains, leading to an increase in the crossover temperature, and allows the precise determination of relaxation times and the energy barrier in the finite size regime.

The ferromagnetic exchange interaction was estimated from an analysis of the specific heat and magnetic susceptibility data by using the Ising chain model. Even though computational studies revealed an easy-axis type of anisotropy of the ground-state Kramers doublets, the question arose as to whether the use of this model is really adequate. To gain a

deeper insight into this topic, a quantitative analysis of the behavior of such $[\text{Co}(\text{NCS})_2\text{L}_2]_n$ chains was needed that goes beyond the Ising model and has never been made before for this class of compounds. Therefore, we used the more general XXZ Heisenberg spin chain model for data analysis, which gave very similar results, thereby proving that the Ising model is a reasonable approximation in this case. In this context, it is noted that the XXZ model can also be used for the analysis of other $s=1/2$ chain systems for which the Ising model is inadequate. This is of extraordinary importance for the overall project, in which a number of linear and corrugated chains have been synthesized and for which the anisotropy has changed dramatically.

Moreover, for the first time, the spin excitation energy has been measured directly by FD-FT THz-EPR spectroscopy. This leads to significant differences in the values obtained by specific heat and magnetic measurements, which can also be explained by using the more general XXZ model. The anisotropy of the exchange interaction J_{xx}/J_{zz} estimated from ab initio wave functions and $J_{zz}-J_{xx}$ derived from EPR spectroscopy lead to a spin Hamiltonian that nicely reproduces the specific heat and susceptibility data.

Finally, the energy needed for the nucleation of a domain wall, Δ_S , retrieved from ac measurements and by using the XXZ model, also leads to perfect agreement. However, the question about the absolute values of the energy barriers, and their relation to the single-ion anisotropy barrier, remains and will be the subject of future investigations.

Experimental Section

$\text{Co}(\text{NCS})_2$ was obtained from Sigma–Aldrich and 4-methoxypyridine from TCI. All reactions were carried out under ambient conditions. After the reaction, the residue was filtered off and dried in air unless noted otherwise. The purity of all compounds was verified by PXRD analysis.

Synthesis of $[\text{Co}(\text{NCS})_2(4\text{-methoxypyridine})_2]_n$ (1)

Compound **1** was prepared by mixing $\text{Co}(\text{NCS})_2$ (0.5 mmol, 87.6 mg) and 4-methoxypyridine (0.75 mmol, 76.2 μL) in ethanol (0.5 mL) with stirring for 2 h. Single crystals were grown by the slow evaporation of a solution of $\text{Co}(\text{NCS})_2$ (0.25 mmol, 43.8 mg) and 4-methoxypyridine (0.25 mmol, 25.4 μL) in ethanol (2.0 mL). Elemental analysis calcd (%) for $\text{C}_{14}\text{H}_{14}\text{N}_4\text{CoO}_2\text{S}_2$ (393.356): C 42.75, H 3.59, N 14.24, S 16.30; found: C 42.64, H 3.54, N 13.90, S 16.86.

Synthesis of $[\text{Co}(\text{NCS})_2(4\text{-methoxypyridine})_4]_n$ (2)

Compound **2** was prepared by mixing $\text{Co}(\text{NCS})_2$ (0.5 mmol, 87.6 mg) and 4-methoxypyridine (4.00 mmol, 406 μL) in water (3.0 mL) with stirring for 2 d and the residue was washed with water. Elemental analysis calcd (%) for $\text{C}_{26}\text{H}_{28}\text{N}_6\text{CoO}_4\text{S}_2$ (611.611): C 51.06, H 4.61, N 13.74, S 10.49; found: C 50.88, H 4.48, N 10.63, S 10.23.

Synthesis of $[\text{Co}(\text{NCS})_2(4\text{-methoxypyridine})_2]_n$ (3)

A solution of 4-methoxypyridine (0.50 mmol, 50.8 μL) in water (50 μL) was slowly added to a stirred suspension of $\text{Co}(\text{NCS})_2$

(1.0 mmol, 175.2 mg) in water (0.3 mL) and the mixture stirred thoroughly for 2 min. The residue was filtered off and washed with *n*-heptane. Elemental analysis calcd (%) for $\text{C}_{14}\text{H}_{14}\text{N}_4\text{CoO}_2\text{S}_2$ (393.356): C 42.75, H 3.59, N 14.24, S 16.30; found: C 41.98, H 3.37, N 14.22, S 16.99.

Elemental analysis

CHNS analysis was performed by using an EURO EA elemental analyzer, fabricated by EURO VECTOR Instruments.

IR spectroscopy

The IR spectra were recorded by using an ATI Mattson Genesis Series FTIR spectrometer (control software: WINFIRST, from ATI Mattson).

Powder X-ray diffraction

PXRD measurements were performed with $\text{Cu}_{K\alpha 1}$ radiation ($\lambda = 1.540598 \text{ \AA}$) using a Stoe Transmission Powder Diffraction System (STADI P) equipped with a MYTHEN 1K detector and a Johansson-type Ge(111) monochromator.

Single-crystal XRD analysis

Data collection was performed with an imaging plate diffraction system (IPDS-2) from STOE & CIE using $\text{Mo}_{K\alpha}$ radiation. Structure solution was performed with SHELXS-97^[26] and structure refinement was performed against F^2 using SHELXL-2014.^[27] A numerical absorption correction was applied by using the X-RED and X-SHAPE programs of the X-AREA program package.^[28] All non-hydrogen atoms were refined by using anisotropic displacement parameters. All C–H hydrogen atoms were positioned with idealized geometries (methyl H atoms were allowed to rotate but not to tip) and refined isotropically by using the expression $U_{\text{iso}}(\text{H}) = 1.2U_{\text{eq}}(\text{C})$ ($1.5U_{\text{eq}}(\text{C})$ for the methyl H atoms) using a riding model. Selected crystal data and details of the structure refinements can be found in Table 1.

CCDC 1948119 contains the supplementary crystallographic data for this paper. These data are provided free of charge by The Cambridge Crystallographic Data Centre.

Magnetic measurements

Magnetic measurements were performed on polycrystalline samples by using a Quantum Design MPMS XL magnetometer. Powder samples were frozen in mineral oil in zero magnetic field. Diamagnetic corrections of the core diamagnetism and sample holder were subtracted. For ac susceptibility measurements, a phase correction was applied based on frequency-dependent calibrations made with a paramagnetic Gd_2O_3 sample. Temperatures in the range 2.2–4 K were measured by using a thermometer close to the sample, and verified by using a paramagnetic sample as thermometer.

Specific heat measurements

Specific heats were measured by the relaxation technique using a Quantum Design PPMS instrument. A powder sample was pressed without any binder into a thin pellet. Apiezon N grease was used to fix the sample. The heat capacities of the grease and calorimeter were determined before measurements of the samples and subtracted.

Computational details

All DFT calculations were performed with the TURBOMOLE package of programs.^[29] The structural models used were based on the single-crystal X-ray structure data of **1**. For all computational models, the positions of the hydrogen atoms were optimized at the RI-DFT^[30]/BP86^[31]/def2-SVP^[32] level of theory. Within these optimizations, cobalt(II) was replaced by zinc(II) to achieve a faster SCF convergence and thus decrease the computational effort. The single-ion properties of the cobalt centers of **1** were obtained by high-level ab initio calculations using the Molcas 8.0 SP1^[21] package of programs. The calculations were based on the mononuclear cobalt(II) structural model [CoZn₂(NCS)₆(4-methoxypyridine)₂]²⁺ for the two crystallographically independent centers (denoted as **1-Co1** and **1-Co2**). The two additional zinc(II) ions in the computational models at the actual positions of the neighboring cobalt(II) ions were necessary to counterbalance the dianionic charge of the fragment, which otherwise can lead to convergence problems. Relativistic effects were taken into account by a second-order Douglas-Kroll-Hess Hamiltonian in combination with ANO-RCC basis sets^[33] (Co and donor atoms: ANO-RCC-VTZP; remaining atoms: ANO-RCC-VDZ). CASSCF calculations on **1-Co1** and **1-Co2** were carried out for 10 quartet (⁴F, ⁴P) and 40 doublet states (²G, ²P, ²H, ²D, ²D, ²F) with an active space consisting of 7 electrons in 10 orbitals (3d and 4d) to adequately take the "double d-shell effect" into account.^[34] Subsequent CASPT2 calculations based on the CASSCF wave functions involved all the quartet and the 12 lowest doublet states. To include spin-orbit coupling and to treat the mixing of different multiplicities, the RASSI-SO method was employed based on the CASSCF/CASPT2 wave functions. Finally, the SINGLE_ANISO module was used to obtain single-ion anisotropies and the components of the *g* tensor.

The investigation of the magnetic exchange in **1** was based on broken-symmetry DFT (BS-DFT) calculations at the DFT/B3-LYP^[31a,35]/def2-TZVP^[32] level of theory. For these calculations, a dinuclear cobalt(II) computational model [Co₂Zn₂(NCS)₆(4-methoxypyridine)₄]²⁺ (denoted as **1-Co1Co2**) was used. The theoretical magnetic coupling constant *J* was obtained by Yamaguchi's approach^[36] given by Equation (9)

$$J_{12} = \frac{2(E_{BS} - E_{HS})}{\langle S_{HS}^2 \rangle - \langle S_{BS}^2 \rangle} \quad (9)$$

and represents the magnetic coupling between two Heisenberg spins with $\hat{H} = -J_{12}S_1S_2$ and $S = 3/2$.

DMRG simulations

Density matrix renormalization group (DMRG) simulations of the 1D XXZ spin model were performed directly in the thermodynamic limit by using a custom implemented algorithm. This algorithm was based on the representation of the quantum state in the form of a uniform matrix product state (uMPS).^[24] The maximal bond dimension, that is, the size of matrices appearing in uMPS, was used to control the quality of the approximation and acts as a cut-off parameter in the algorithm. To simulate the state at finite temperature we employed the purification approach. The density matrix at finite temperature was obtained by starting with the trivial state at infinite temperature and simulating the imaginary time evolution. The time-dependent variational principle approach was used.^[24c,37] The algorithm used had previously been tested by comparing with Monte Carlo simulations,^[38] simulations for finite spin systems, and analytical formulae known for the limiting cases. The dispersion relation was calculated by using variational uMPS excitation ansatz,

which was constructed on top of the ground state as a superposition of its local perturbations forming a state with given momentum.^[24c,25]

FD-FT THz-EPR spectroscopy

FD-FT THz-EPR spectra were acquired at the THz-EPR user-station of the electron-storage ring BESSY II. The setup is described in detail elsewhere.^[10,39] THz coherent synchrotron radiation (CSR) or broadband, unpolarized THz radiation emitted by the Hg arc lamp of an FTIR spectrometer (Bruker IFS 125) were used as broadband (ca. 4–50 cm⁻¹ and > 12 cm⁻¹, respectively) excitation sources. The radiation was transmitted by a quasi-optical evacuated transmission line through the FTIR spectrometer and focused on the sample contained in a 10 T superconducting magnet (Oxford Spectromag). Spectra were recorded in the Voigt geometry. The transmitted signal was detected with a Si bolometer detector (IR labs) and Fourier-transformed to yield frequency-domain EPR spectra. The experimental resolution was 1 cm⁻¹. Polycrystalline **1** (35 mg for Hg arc and 75 mg for CSR) was homogenized in a mortar with polyethylene (PE) powder (42 or 58 mg, respectively) and pressed into a pellet, which was mounted in the variable-temperature insert of the magnet. To remove the incident background transmission from the spectrum, reference spectra were recorded at either different fields or temperatures.^[10,40] Magnetic-field division spectra (MDS) recorded at two magnetic fields *B_i* and *B_j* are presented as the relative transmittance *T_i* obtained experimentally from the measured spectral intensities *I* according to $T_{exp} = I_{B_i}/I_{B_j}$. Temperature division spectra recorded at two temperatures *T_{ref}* and *T_i* are presented as the relative absorbance according to $A_{exp} = \log_{10}(I_{T_{ref}}/I_{T_i})$.

Acknowledgements

This project was supported by the Deutsche Forschungsgemeinschaft (Project No. Na 720/5-2 and PL 155/16-2), the State of Schleswig-Holstein, and the National Science Centre, Poland (project no. 2017/25/B/ST3/00856). We thank Prof. Dr. W. Bensch for access to his experimental facilities. We are grateful to Dr. K. Holldack and D. Ponwitz for experimental assistance with the FD-FT THz-EPR experiments. Support of the FD-FT THz-EPR experiments through the user program of Helmholtz-Zentrum Berlin and DFG SPP 1601 are gratefully acknowledged.

Conflict of interest

The authors declare no conflict of interest.

Keywords: ab initio calculations · cobalt · EPR spectroscopy · magnetic properties · single-chain magnets

- [1] a) C. Coulon, H. Miyasaka, R. Clérac, *Struct. Bonding* **2006**, *122*, 163–206; b) H.-L. Sun, Z.-M. Wang, S. Gao, *Coord. Chem. Rev.* **2010**, *254*, 1081–1100; c) G. A. Craig, M. Murrie, *Chem. Soc. Rev.* **2015**, *44*, 2135–2147; d) R. Lescaouézec, L. M. Toma, J. Vaissermann, M. Verdaguer, F. S. Delgado, C. Ruiz-Pérez, F. Lloret, M. Julve, *Coord. Chem. Rev.* **2005**, *249*, 2691–2729; e) S. Dhers, H. L. C. Feltham, S. Brooker, *Coord. Chem. Rev.* **2015**, *296*, 24–44; f) C. Coulon, V. Pianet, M. Urdampilleta, R. Clérac in *Molecular Nanomagnets and Related Phenomena*, Vol. 164 (Ed.: S. E. Gao), Springer, Heidelberg, **2015**, pp. 143–184; g) M. Feng, M.-L. Tong, *Chem.*

- Eur. J.* **2018**, *24*, 7574–7594; h) S. Ziegenbalg, D. Hornig, H. Görls, W. Plass, *Inorg. Chem.* **2016**, *55*, 4047–4058; i) J. M. Zadrozny, J. Liu, N. A. Piro, C. J. Chang, S. Hill, J. R. Long, *Chem. Commun.* **2012**, *48*, 3927–3929; j) D. Pinkowicz, H. I. Southerland, C. Avendaño, A. Prosvirin, C. Sanders, W. Wernsdorfer, K. S. Pedersen, J. Dreiser, R. Clérac, J. Nehrkorn, G. G. Simeoni, A. Schnegg, K. Hollmack, K. R. Dunbar, *J. Am. Chem. Soc.* **2015**, *137*, 14406–14422; k) K. S. Pedersen, J. Bendix, R. Clerac, *Chem. Commun.* **2014**, *50*, 4396–4415; l) F. S. Guo, B. M. Day, Y. C. Chen, M. L. Tong, A. Mansikkamaki, R. A. Layfield, *Science* **2018**, *362*, 1400–1403; m) M. J. Heras Ojea, V. A. Milway, G. Velmurugan, L. H. Thomas, S. J. Coles, C. Wilson, W. Wernsdorfer, G. Rajaraman, M. Murrie, *Chem. Eur. J.* **2016**, *22*, 12839–12848; n) J. M. Frost, K. L. M. Harriman, M. Murugesu, *Chem. Sci.* **2016**, *7*, 2470–2491; o) J. Palion-Gazda, T. Klemens, B. Machura, J. Vallejo, F. Lloret, M. Julve, *Dalton Trans.* **2015**, *44*, 2989–2992; p) S. Chorazy, M. Rams, A. Hoczek, B. Czarniecki, B. Sieklucka, S. Ohkoshi, R. Podgajny, *Chem. Commun.* **2016**, *52*, 4772–4775; q) M. Böhme, S. Ziegenbalg, A. Aliabadi, A. Schnegg, H. Görls, W. Plass, *Dalton Trans.* **2018**, *47*, 10861–10873; r) M. A. Palacios, J. Nehrkorn, E. A. Sutturina, E. Ruiz, S. Gómez-Coca, K. Hollmack, A. Schnegg, J. Krzystek, J. M. Moreno, E. Colacio, *Chem. Eur. J.* **2017**, *23*, 11649–11661.
- [2] a) L. Bogani, W. Wernsdorfer, *Nat. Mater.* **2008**, *7*, 179–186; b) M. N. Leuenberger, D. Loss, *Nature* **2001**, *410*, 789–793; c) R. Mas-Ballesté, J. Gómez-Herrero, F. Zamora, *Chem. Soc. Rev.* **2010**, *39*, 4220–4233; d) G. Aromí, D. Aguila, P. Gamez, F. Luis, O. Roubeau, *Chem. Soc. Rev.* **2012**, *41*, 537–546; e) S. G. McAdams, A.-M. Ariciu, A. K. Kostopoulos, J. P. S. Walsh, F. Tuna, *Coord. Chem. Rev.* **2017**, *346*, 216–239; f) K. Y. Monakhov, M. Moors, P. Kögerler in *Polyoxometalate chemistry. Advances in Inorganic Chemistry, Vol. 69* (Eds.: R. van Eldik, L. Cronin), Academic Press, Cambridge, **2017**, pp. 251–286; g) J. Liu, J. Mrozek, W. K. Myers, G. A. Timco, R. E. P. Winpenny, B. Kintzel, W. Plass, A. Ardavan, *Phys. Rev. Lett.* **2019**, *122*, 037202.
- [3] a) X. Feng, J. Liu, T. D. Harris, S. Hill, J. R. Long, *J. Am. Chem. Soc.* **2012**, *134*, 7521–7529; b) W.-X. Zhang, T. Shiga, H. Miyasaka, M. Yamashita, *J. Am. Chem. Soc.* **2012**, *134*, 6908–6911; c) E. V. Peresyapkina, A. M. Majcher, M. Rams, K. E. Vostrikova, *Chem. Commun.* **2014**, *50*, 7150–7153; d) Z. Tomkowicz, M. Rams, M. Bañanda, S. Foro, H. Nojiri, Y. Krupskaya, V. Kataev, B. Büchner, S. K. Nayak, J. V. Yakhmi, W. Haase, *Inorg. Chem.* **2012**, *51*, 9983–9994; e) H. Miyasaka, T. Madanbashi, K. Sugimoto, Y. Nakazawa, W. Wernsdorfer, K.-i. Sugiura, M. Yamashita, C. Coulon, R. Clérac, *Chem. Eur. J.* **2006**, *12*, 7028–7040; f) H. Miyasaka, K. Takayama, A. Saitoh, S. Furukawa, M. Yamashita, R. Clérac, *Chem. Eur. J.* **2010**, *16*, 3656–3662; g) S. Wöhlert, U. Ruschewitz, C. Näther, *Cryst. Growth Des.* **2012**, *12*, 2715–2718; h) R. Liu, L. Li, X. Wang, P. Yang, C. Wang, D. Liao, J.-P. Sutter, *Chem. Commun.* **2010**, *46*, 2566–2568; i) E. Pardo, C. Train, R. Lescouezec, Y. Journaux, J. Pasan, C. Ruiz-Perez, F. S. Delgado, R. Ruiz-García, F. Lloret, C. Paulsen, *Chem. Commun.* **2010**, *46*, 2322–2324; j) V. Tangoulis, M. Lalia-Kantouri, M. Gdaniec, C. Papadopoulos, V. Miletic, A. Czapik, *Inorg. Chem.* **2013**, *52*, 6559–6569; k) N. Hoshino, Y. Sekine, M. Nihei, H. Oshio, *Chem. Commun.* **2010**, *46*, 6117–6119; l) E. Coronado, J. R. Galan-Mascarós, C. Martí-Gastaldo, *J. Am. Chem. Soc.* **2008**, *130*, 14987–14989.
- [4] S. Wöhlert, J. Boeckmann, M. Wriedt, C. Näther, *Angew. Chem. Int. Ed.* **2011**, *50*, 6920–6923; *Angew. Chem.* **2011**, *123*, 7053–7056.
- [5] a) S. Wöhlert, Z. Tomkowicz, M. Rams, S. G. Ebbinghaus, L. Fink, M. U. Schmidt, C. Näther, *Inorg. Chem.* **2014**, *53*, 8298–8310; b) J. Werner, Z. Tomkowicz, M. Rams, S. G. Ebbinghaus, T. Neumann, C. Näther, *Dalton Trans.* **2015**, *44*, 14149–14158; c) S. Wöhlert, T. Fic, Z. Tomkowicz, S. G. Ebbinghaus, M. Rams, W. Haase, C. Näther, *Inorg. Chem.* **2013**, *52*, 12947–12957.
- [6] a) M. Rams, M. Böhme, V. Kataev, Y. Krupskaya, B. Büchner, W. Plass, T. Neumann, Z. Tomkowicz, C. Näther, *Phys. Chem. Chem. Phys.* **2017**, *19*, 24534–24544; b) J. Werner, M. Rams, Z. Tomkowicz, C. Näther, *Dalton Trans.* **2014**, *43*, 17333–17342; c) J. Boeckmann, C. Näther, *Dalton Trans.* **2010**, *39*, 11019–11026; d) J. Werner, M. Rams, Z. Tomkowicz, T. Runčevski, R. E. Dinnebier, S. Suckert, C. Näther, *Inorg. Chem.* **2015**, *54*, 2893–2901; e) T. Neumann, M. Rams, Z. Tomkowicz, I. Jess, C. Näther, *Chem. Commun.* **2019**, *55*, 2652–2655.
- [7] M. Rams, Z. Tomkowicz, M. Böhme, W. Plass, S. Suckert, J. Werner, I. Jess, C. Näther, *Phys. Chem. Chem. Phys.* **2017**, *19*, 3232–3243.
- [8] S. Baran, A. Hoser, M. Rams, S. Ostrovsky, T. Neumann, C. Näther, Z. Tomkowicz, *J. Phys. Chem. Solids* **2019**, *130*, 290–297.
- [9] F. A. Mautner, M. Traber, R. C. Fischer, A. Torvisco, K. Reichmann, S. Speed, R. Vicente, S. S. Massoud, *Polyhedron* **2018**, *154*, 436–442.
- [10] J. Nehrkorn, K. Hollmack, R. Bittl, A. Schnegg, *J. Magn. Reson.* **2017**, *280*, 10–19.
- [11] C. Näther, S. Wöhlert, J. Boeckmann, M. Wriedt, I. Jess, *Z. Anorg. Allg. Chem.* **2013**, *639*, 2696–2714.
- [12] T. Neumann, I. Jess, F. Pielhofer, C. Näther, *Eur. J. Inorg. Chem.* **2018**, 4972–4981.
- [13] R. L. Carlin, *Magnetochemistry*, Springer, New York, **1986**.
- [14] C. Coulon, R. Clérac, W. Wernsdorfer, T. Colin, H. Miyasaka, *Phys. Rev. Lett.* **2009**, *102*, 167204.
- [15] a) M. Pinsky, D. Avnir, *Inorg. Chem.* **1998**, *37*, 5575–5582; b) H. Zabrodsky, S. Peleg, D. Avnir, *IEEE Trans. Pattern Anal.* **1995**, *17*, 1154–1166.
- [16] a) Y. Oshima, H. Nojiri, K. Asakura, T. Sakai, M. Yamashita, H. Miyasaka, *Phys. Rev. B* **2006**, *73*, 214435; b) A. Amjad, G. M. Espallargas, J. Liu, J. M. Clemente-Juan, E. Coronado, S. Hill, E. del Barco, *Polyhedron* **2013**, *66*, 218–221.
- [17] L. A. Bosch, G. J. P. M. Lauwers, K. Kopinga, C. Vandersteen, W. J. M. Dejonge, *J. Phys. C* **1987**, *20*, 609–627.
- [18] a) J. B. Torrance, M. Tinkham, *Phys. Rev.* **1969**, *187*, 587; b) M. Elmassalami, L. J. Dejongh, *Physica B* **1989**, *154*, 254–266.
- [19] J. Nehrkorn, S. L. Veber, L. A. Zhukas, V. V. Novikov, Y. V. Nelyubina, Y. Z. Voloshin, K. Hollmack, S. Stoll, A. Schnegg, *Inorg. Chem.* **2018**, *57*, 15330–15340.
- [20] M. E. Lines, *J. Chem. Phys.* **1971**, *55*, 2977–2984.
- [21] a) F. Aquilante, J. Autschbach, R. K. Carlson, L. F. Chibotaru, M. G. Delcey, L. D. Vico, I. F. Galván, N. Ferré, L. M. Frutos, L. Gagliardi, M. Garavelli, A. Giussani, C. E. Hoyer, G. L. Manni, H. Lischka, D. Ma, P. Å. Malmqvist, T. Müller, A. Nenov, M. Olivucci, T. B. Pedersen, D. Peng, F. Plasser, B. Pritchard, M. Reiher, I. Rivalta, I. Schapiro, J. Segarra-Martí, M. Stenrup, D. G. Truhlar, L. Ungur, A. Valentini, S. Vancocillie, V. Varyazov, V. P. Vysotskiy, O. Weingart, F. Zapata, R. Lindh, *J. Comput. Chem.* **2016**, *37*, 506–541; b) F. Aquilante, L. D. Vico, N. Ferré, G. Ghigo, P.-Å. Malmqvist, P. Neogrady, T. B. Pedersen, M. Pitoňák, M. Reiher, B. O. Roos, L. Serrano-Andrés, M. Urban, V. Varyazov, R. Lindh, *J. Comput. Chem.* **2010**, *31*, 224–247; c) G. Karlström, R. Lindh, P.-Å. Malmqvist, B. O. Roos, U. Ryde, V. Varyazov, P.-O. Widmark, M. Cossi, B. Schimmelpfennig, P. Neogrady, L. Seijo, *Comp. Mater. Sci.* **2003**, *28*, 222–239; d) V. Varyazov, P.-O. Widmark, L. Serrano-Andrés, R. Lindh, B. O. Roos, *Int. J. Quantum Chem.* **2004**, *100*, 626–635.
- [22] J. C. Bonner, M. E. Fisher, *Phys. Rev.* **1964**, *135*, A640.
- [23] M. Takahashi, *Thermodynamics of One-Dimensional Solvable Models*, Cambridge University Press, Cambridge, **1999**.
- [24] a) F. Verstraete, V. Murg, J. I. Cirac, *Adv. Phys.* **2008**, *57*, 143–224; b) U. Schollwöck, *Ann. Phys.* **2011**, *326*, 96–192; c) L. Vanderstraeten, J. Haegeman, F. Verstraete, *SciPost Phys. Lect. Notes* **2019**, *7*.
- [25] J. Haegeman, S. Michalakis, B. Nachtergaele, T. J. Osborne, N. Schuch, F. Verstraete, *Phys. Rev. Lett.* **2013**, *111*, 080401.
- [26] SHELXS-97 1997, University of Göttingen.
- [27] G. M. Sheldrick, *Acta Crystallogr. C* **2015**, *71*, 3–8.
- [28] a) X-RED 1.11, 1998, STOE & CIE GmbH; b) X-SHAPE 1.03, 1998, STOE & CIE GmbH; c) X-AREA 1.44, 2008, STOE & CIE GmbH.
- [29] TURBOMOLE V7.2 2017, a development of University of Karlsruhe and Forschungszentrum Karlsruhe GmbH, 1989–2007, TURBOMOLE GmbH, since 2007; available from <http://www.turbomole.com>.
- [30] a) E. J. Baerends, D. E. Ellis, P. Ros, *Chem. Phys.* **1973**, *2*, 41–51; b) B. I. Dunlap, J. W. D. Connolly, J. R. Sabin, *J. Chem. Phys.* **1979**, *71*, 3396–3402; c) C. Van Alsenoy, *J. Comput. Chem.* **1988**, *9*, 620–626; d) J. L. Whitten, *J. Chem. Phys.* **1973**, *58*, 4496–4501.
- [31] a) A. D. Becke, *Phys. Rev. A* **1988**, *38*, 3098–3100; b) J. P. Perdew, *Phys. Rev. B* **1986**, *33*, 8822–8824.
- [32] F. Weigend, R. Ahlrichs, *Phys. Chem. Chem. Phys.* **2005**, *7*, 3297–3305.
- [33] a) B. O. Roos, R. Lindh, P.-Å. Malmqvist, V. Varyazov, P.-O. Widmark, *J. Phys. Chem. A* **2004**, *108*, 2851–2858; b) B. O. Roos, R. Lindh, P.-Å. Malmqvist, V. Varyazov, P.-O. Widmark, *J. Phys. Chem. A* **2005**, *109*, 6575–6579; c) P.-O. Widmark, P.-Å. Malmqvist, B. O. Roos, *Theor. Chim. Acta* **1990**, *77*, 291–306.
- [34] K. Andersson, B. O. Roos, *Chem. Phys. Lett.* **1992**, *191*, 507–514.
- [35] A. D. Becke, *J. Chem. Phys.* **1993**, *98*, 5648–5652.
- [36] a) T. Soda, Y. Kitagawa, T. Onishi, Y. Takano, Y. Shigeta, H. Nagao, Y. Yoshioka, K. Yamaguchi, *Chem. Phys. Lett.* **2000**, *319*, 223–230; b) K. Yamagu-

- chi, T. Tsunekawa, Y. Toyoda, T. Fueno, *Chem. Phys. Lett.* **1988**, *143*, 371–376.
- [37] J. Haegeman, J. I. Cirac, T. J. Osborne, I. Pižorn, H. Verschelde, F. Verstraete, *Phys. Rev. Lett.* **2011**, *107*, 070601.
- [38] S. Suckert, M. Rams, M. M. Rams, C. Näther, *Inorg. Chem.* **2017**, *56*, 8007–8017.
- [39] K. Holldack, A. Schnegg, *JLSRF* **2016**, *2*, A51.
- [40] J. Nehr Korn, B. M. Martins, K. Holldack, S. Stoll, H. Dobbek, R. Bittl, A. Schnegg, *Mol. Phys.* **2013**, *111*, 2696–2707.

Manuscript received: August 27, 2019

Accepted manuscript online: November 8, 2019

Version of record online: January 9, 2020